Journal of Advanced Ceramics
2023, **12**(9): 1685–1700
https://doi.org/10.26599/JAC.2023.9220758
ISSN 2226-4108
CN 10-1154/TQ

Research Article

$SnFe_2O_4/ZnIn_2S_4$/PVDF piezophotocatalyst with improved photocatalytic hydrogen production by synergetic effects of heterojunction and piezoelectricity

Ping Su[a], Dezhi Kong[a], Huaihao Zhao[a], Shangkun Li[a], Dafeng Zhang[a,*], Xipeng Pu[a,*], Changhua Su[a], Peiqing Cai[b]

[a]*School of Materials Science and Engineering, Shandong Key Laboratory of Chemical Energy Storage and New Battery Technology, Liaocheng University, Liaocheng 252000, China*
[b]*College of Optical and Electronic Technology, China Jiliang University, Hangzhou 310018, China*

Received: January 14, 2023; Revised: April 2, 2023; Accepted: April 24, 2023
© The Author(s) 2023.

Abstract: The polarized electric field inside piezoelectric materials has been proven to be a promising technique to boost photogenerated charge separation. Herein, a novel flexible $SnFe_2O_4/ZnIn_2S_4$/polyvinylidene fluoride ($(CH_2CF_2)_n$, PVDF) (P–SZ) film piezophotocatalyst was successfully synthesized by combining PVDF, an organic piezoelectric material, with a $SnFe_2O_4/ZnIn_2S_4$ (SFO/ZIS) type II heterojunction photocatalyst. The hydrogen evolution rate of SFO/ZIS heterojunction with a SFO content of 5% is about 846.79 $\mu mol \cdot h^{-1} \cdot g^{-1}$, which is 3.6 times that of pristine ZIS. Furthermore, after being combined with PVDF, the optimum hydrogen evolution rate of P–SZ is about 1652.7 $\mu mol \cdot h^{-1} \cdot g^{-1}$ in the presence of ultrasound, which exceeds that of 5% SFO/ZIS by an approximate factor of 2.0. Based on experimental results, the mechanism of the improved photocatalytic performance of P–SZ was proposed on the basis of the piezoelectric field in PVDF and the formed heterojunction between SFO and ZIS, which effectively boosted the separation of photoinduced charges. This work provides an efficient strategy for multi-path collection and utilization of natural solar and vibrational energy to enhance photoactivity.

Keywords: heterojunction; piezophotocatalysis; $SnFe_2O_4$ (SFO); $ZnIn_2S_4$ (ZIS); polyvinylidene fluoride ($(CH_2CF_2)_n$, PVDF) film

1 Introduction

In recent decades, severe environmental and energy crises are two major problems that need to be urgently solved for social green and low-carbon development [1–3]. Photocatalysis technology over semiconductors has gradually become a research hotspot all over the world owing to the utilization of almost free and clean solar energy resources, which provided an effective avenue to relieve the above severe menaces [4,5].

$ZnIn_2S_4$ (ZIS), as a layered ternary metal chalcogenide, exhibits promising potential due to its suitable energy band positions, superior visible light responsiveness, and excellent chemical stability [6]. Its unique ultrathin staggered layered structure endows it with a large

* Corresponding authors.
E-mail: D. Zhang, dafengzh@hotmail.com;
X. Pu, xipengpu@hotmail.com

contact-specific surface area, which greatly shortens a diffusion path of photogenerated carriers [7,8]. At the same time, it is vulnerable to the photocorrosion and high recombination rate of electron–hole pairs [9], which limit its applications in the field of photocatalysis. To solve these shortcomings, numerous works such as ion doping [10], precious metal deposition [11], and construction of heterojunction [12] have been widely carried out. Currently, the compound semiconductor strategy is the mostly used method to improve the photocatalytic performance of ZIS, which can promote charge separation by the formed heterojunction between components. Wang *et al*. [13] constructed a ZIS/Ir_2S_3 composite heterojunction photocatalyst by a one-step hydrothermal method, which generated the built-in electric field between ZIS and Ir_2S_3. Yang *et al*. [14] used an electrostatic self-assembly method to prepare a strongly coupled photocatalyst consisting of g-C_3N_4 and ZIS. The close contact of the heterostructure promoted the transfer and separation of charge carriers.

Spinel ferrite $SnFe_2O_4$ (SFO) is commonly used in various photocatalytic systems due to its high visible light activity, low cost, and non-toxicity [15], whereas there is little research in the field of photocatalytic hydrogen evolution. SFO usually grows into zero-dimensional (0D) nanoparticles, which can provide more active sites on the surface of the photocatalyst and reduce the recombination of photo-induced carriers after being coupled with other photocatalysts [16]. Based on the above advantages, SFO and ZIS were reasonably prepared into $SnFe_2O_4$/$ZnIn_2S_4$ (SFO/ZIS) heterojunction photocatalysts by a simple ultrasonic self-assembly method, combined with morphological characteristics and suitable band edge positions of ZIS and SFO nanoparticles [17,18]. However, such powder photocatalysts usually exist as suspended particles in the reaction system and require significant efforts to separate and recover them after photocatalysis.

Recently, the piezoelectric field has been gradually applied in the field of the photocatalysis due to its ability to accelerate the directional separation and transfer of the charge carriers [19,20]. Piezoelectric materials can be deformed under the action of stress such as mechanical stirring or ultrasonic vibration, and noncoincidence of charge centers will generate an alternating polarized electric field [21]. Consequently, electrons and holes can be rapidly separated to the two ends of the photocatalyst by the change of the potential in the piezoelectric field, thereby successfully improving the charge transfer behavior on its surface [22,23]. Generally, most reports have focused on efforts to develop piezoelectric fields induced by inorganic piezoelectric powders. However, most of the inorganic piezoelectric materials are brittle to a certain extent and have inherent obstacles such as difficulty in recycling, noise, and environmental pollution, which greatly limit their practical applications in photocatalysis [24,25]. As we all know, the organic piezoelectric film polyvinylidene fluoride ($(CH_2CF_2)_n$, PVDF) is one of the polymer materials with exceptional piezoelectric properties [26]. The PVDF film shows superior mechanical properties, great flexibility, high piezoelectricity and chemical stability, light weight and thin texture, as well as easy separation and collection performance, which is more in line with the requirements of sustainable development [27,28]. Wan *et al*. [29] have fabricated piezoelectric catalytic water-cleaning films by embedding $BaTiO_3$ into PVDF. Yin *et al*. [30] have introduced PVDF into the MoS_2/g-C_3N_4 heterojunction to study the effect of piezoelectricity on the catalytic performance of multicomponent photocatalysts. As an excellent substrate material for the photocatalyst films, PVDF has broad application prospects in improving photocatalytic activity.

Hence, in this work, the SFO/ZIS heterojunction photocatalyst was prepared by an ultrasonic self-assembly method. Furtherly, the piezoelectric PVDF was then coupled with the as-obtained SFO/ZIS heterojunction by a simple spin coating method, obtaining a flexible $SnFe_2O_4$/$ZnIn_2S_4$/PVDF (P–SZ) film piezophotocatalyst. Under the action of different mechanical external forces, the piezoelectric field formed by PVDF and the SFO/ZIS heterojunction worked together to boost the effective separation of the photogenerated electrons and holes, resulting in enhanced photocatalytic performance and excellent recyclability. The plausible mechanism and migration process of the photo-introduced carriers were further proposed and discussed.

2 Experimental

2.1 Materials

Deionized (DI) water was used throughout the experiment. PVDF was bought from Sigma-Aldrich Trading Co., Ltd. (China). Stannous chloride ($SnCl_2$), ferrous chloride tetrahydrate ($FeCl_2·4H_2O$), zinc chloride ($ZnCl_2$), indium(III) chloride tetrahydrate ($InCl_3·4H_2O$), thioacetamide (CH_3CSNH_2, TAA), and N,N-dimethylformamide (C_3H_7NO,

DMF) were purchased from Aladdin Co., Ltd., China. All reagents used in this study were of analytical reagent grade without further purification.

2.1.1 Preparation of SFO and ZIS

SFO was prepared by the solvothermal method. In a typical process, 0.85 mmol $SnCl_2$ and 1.7 mmol $FeCl_2{\cdot}4H_2O$ were added to 50 mL ethylene glycol. The pH of the above solution was adjusted to about 10 with 6 M NaOH solution and stirred for 30 min. Thereafter, the solution was transferred into an 80 mL Teflon-lined stainless-steel autoclave and heated at 200 ℃ for 15 h. After naturally cooling to room temperature, the obtained sample was washed several times with DI water and ethanol. Finally, the resulting product was dried overnight at 60 ℃.

For the synthesis of ZIS, 1 mmol $ZnCl_2$, 2 mmol $InCl_3{\cdot}4H_2O$, and 2 mmol TAA were dissolved in 70 mL DI water and stirred vigorously for 30 min at room temperature. Thereafter, the solution was transferred into a 100 mL Teflon-lined stainless-steel autoclave, which was sealed and heated at 120 ℃ for 2 h. After cooling to room temperature, the sample was collected and washed several times with DI water and absolute ethanol, and then dried overnight at 60 ℃.

2.1.2 Preparation of SFO/ZIS heterojunctions

The SFO/ZIS heterojunctions were prepared by an ultrasonic self-assembly method. During the synthesis, the dosage of ZIS samples was fixed, and a series of SFO/ZIS heterojunction structures with different mass ratios (labeled as x, x = 1%, 3%, 5%, 10%, and 15%) of SFO relative to the dosage of ZIS were prepared, which were denoted as x SFO/ZIS. In a typical synthesis procedure for 1% SFO/ZIS, 0.5 g ZIS sample and 0.005 g SFO sample (1%) were suspended into 50 mL DI water, and ultrasonically treated for 1 h. Afterwards, the powders were collected by centrifugation and dried in an oven (DHG-9070A, Shanghai Yiheng Scientific Instrument Co., Ltd., China) at 80 ℃ for 12 h.

2.1.3 Preparation of P–SZ film piezophotocatalysts

The PVDF-based film piezophotocatalysts were prepared by the spin-coating method, as shown in Fig. 1. Typically, 0.5 g PVDF was dispersed in 5 mL DMF. After continuous vigorous stirring for 2 h, transparent homogeneous solution was formed. Thereafter, 0.3 g x SFO/ZIS powders were added, followed by stirring of 1 h. The mixed suspension was coated on glass slides by a spin coater (VTC-100PA, Beijing Sedekase Electronic Co., Ltd., China), and the resulting composite film was cured in an oven at 60 ℃ for 3 min. The film was named as P–x SZ. For comparison, pure PVDF film, P–SFO film, and P–ZIS film were all prepared in a similar condition, except adding nothing, SFO, and ZIS, respectively.

2.2 Photocatalytic measurement

Entire photocatalytic hydrogen production reaction was carried out on a photocatalytic online test system (CEL-SPH2N-D9, Beijing China Education AU-Light Co., Ltd., China). Typically, 10 thin films about 2.5 cm × 2.5 cm in size were dispersed into 100 mL sacrificial solution (0.35 M Na_2S and 0.25 M Na_2SO_3) with continuous stirring. Afterwards, a 300 W xenon lamp was used to irradiate the reactor (CEL-SPH2N, Beijing China Education Au-Light Technology Co., Ltd., China) through a 400 nm cut-off filter (CEL-UVIRCUT400, Beijing China Education Au-Light Technology Co., Ltd., China), and the active area of the reaction was about 16 cm^2. The amount of hydrogen produced at each time was measured by a

Fig. 1 Schemes of synthesis procedure of P–SZ film.

gas chromatograph (GC-7900 Beijing China Education AU-Light Co., Ltd., China). Apparent quantum efficiencies (AQEs) of the thin film photocatalyst associated with different band-pass filters (420, 450, 500, and 600 nm) are calculated by Eq. (1) [31]:

$$\begin{aligned}\mathrm{AQE} &= \frac{2\times \text{Number of evolved hydrogen molecules}}{\text{Number of incident photons}}\times 100\% \\ &= \frac{2NN_{\mathrm{A}}hc}{SIt\lambda}\times 100\% \end{aligned} \quad (1)$$

where N is the number of H_2 molecules, N_A is the Avogadro constant, S is the area of light irradiation, I is the illumination intensity, h is the Planck constant, c is the speed of light, t is the illumination time, and λ is the wavelength of different filters.

Specific details of material characterization as well as photoelectron chemical measurements are provided in Section S1 in the Electronic Supplementary Material (ESM).

3 Results and discussion

3. 1 Physicochemical properties

Figure 2(a) shows X-ray diffraction (XRD) patterns of the samples. The typical diffraction peaks of ZIS can be found at 21.1°, 27.7°, 47.5°, 52.4°, and 56.4°, indexed as the (006), (102), (110), (116), and (002) crystal facets of hexagonal ZIS (JCPDS No. 65-2023), respectively [32]. The diffraction profile of SFO is consistent with that of spinel phase Fe_3O_4 (JCPDS No. 11-0614) since there is no JCPDS available for SFO [33]. Simultaneously, the XRD peaks at 30.09°, 35.48°, 43.12°, 56.98°, and 62.62° can be indexed as the (220), (311), (400), (511), and (440) diffraction planes, respectively [15,34]. In the XRD patterns of SFO/ZIS composites, two sets of profiles corresponding to ZIS and SFO can be observed. As shown in Fig. 2(b), the naked PVDF film shows a strong peak at about 20.5°, which suggests that this film is mainly from a β phase with the piezoelectric property [35]. After a combination of PVDF and SFO/ZIS, the characteristic peak of PVDF can be distinctly observed, indicating that the addition of SFO and ZIS has little impact on the crystalline structure of the PVDF film. Additionally, characteristic diffraction peaks of ZIS of SFO can be observed in the P–SZ films, confirming the successful synthesis of the SFO/ZIS heterojunctions.

Morphologies of the as-obtained ZIS, SFO, 5% SFO/ZIS, and P–5% SZ film piezophotocatalysts were researched by scanning electron microscopy (SEM) images. As shown in Fig. 3(a), the morphology of ZIS is approximately in the form of a regular microsphere composed of ultrathin and smooth interlaced nanosheets. Figure 3(b) shows that pure SFO exhibits the morphology of nanoparticles. Concerning 5% SFO/ZIS (Figs. 3(c) and 3(d)), the micro-spherical morphology was inherited from ZIS with uniform loading of the SFO particles in the gaps of the ZIS nanosheets. It is noted that this structure can provide more interfaces and active sites for photocatalytic reactions. Additionally, the utilization of light can be improved through reflection or scattering between the nanosheets [36]. As a consequence, the SFO/ZIS heterojunction is expected to have the improved photocatalytic hydrogen production performance. In the case of a P–5% SZ film (Figs. 3(e) and 3(f)), many annular structures uniformly exist on the surface of the film. After carefully checking, they are the exposed 5%

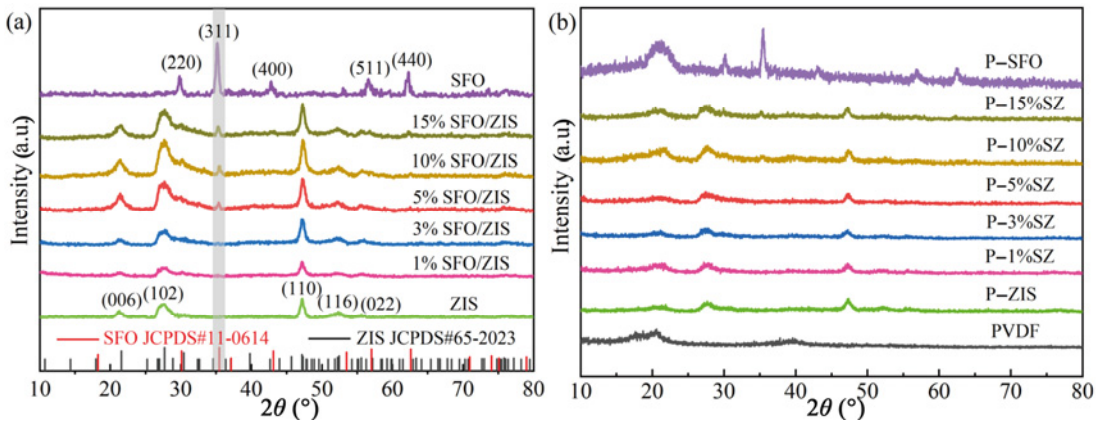

Fig. 2 XRD patterns of (a) ZIS, SFO, and SFO/ZIS and (b) PVDF, P–SFO, P–ZIS, and P–SZ films.

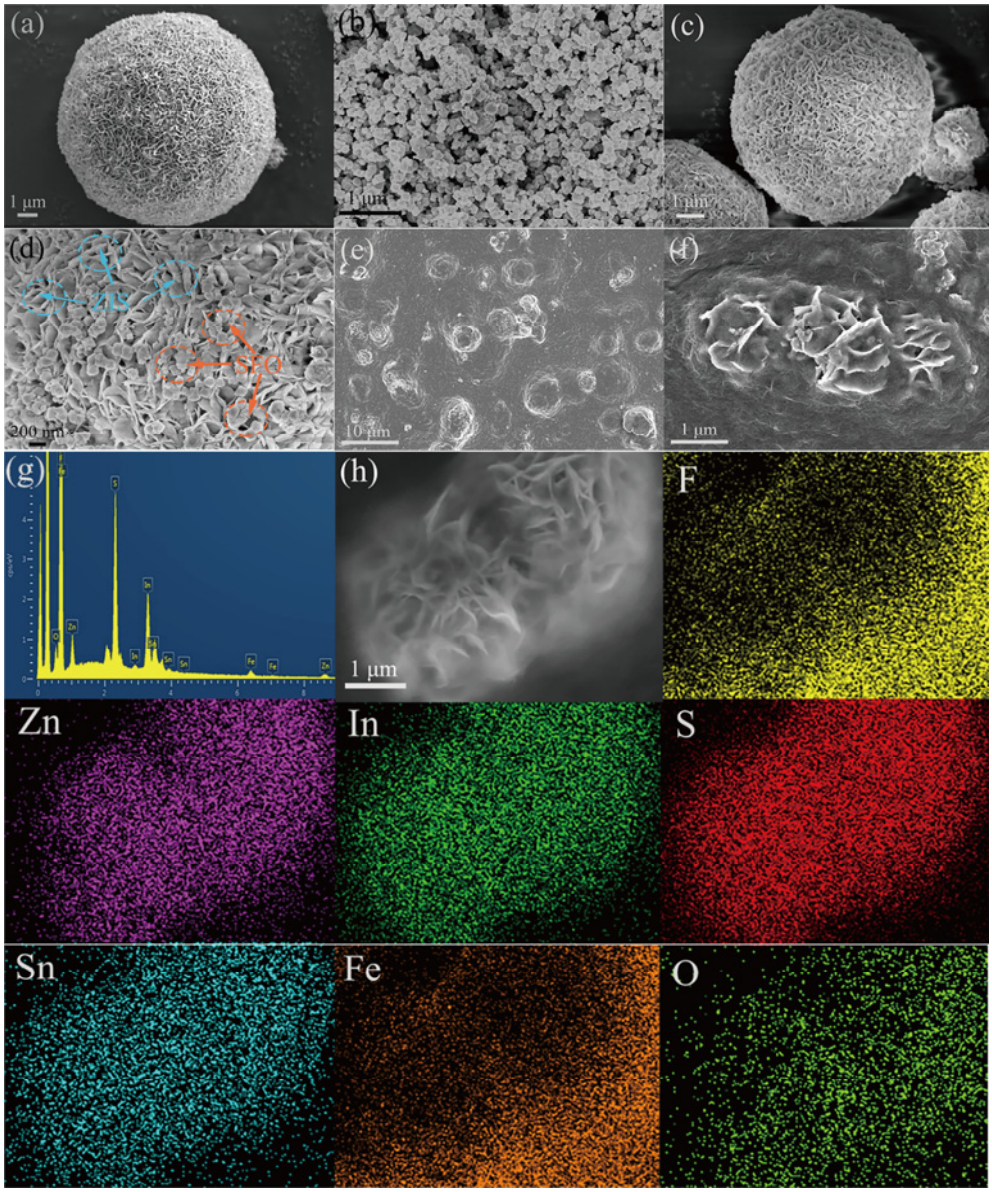

Fig. 3 SEM images of (a) ZIS, (b) SFO, (c, d) 5% SFO/ZIS, and (e, f) P–5% SZ film and (g) EDS reaults and (h) elemental mappings of P–5% SZ film.

SFO/ZIS spheres embedded in PVDF. Apparently, the morphology of SFO/ZIS was not altered during the fabrication of the P–SZ film; moreover, the interface between PVDF and 5% SFO/ZIS was apparently tight. Elemental mappings and energy dispersive X-ray spectroscopy (EDS) of the P–5% SZ film were tested, as depicted in Figs. 3(h) and 3(g), respectively. Apparently, F, Zn, In, S, Sn, Fe, and O can be found in EDS. The F element and other elements show complementary distributions, confirming the successful synthesis of the P–5% SZ film piezophotocatalyst.

To further observe microstructure details of the ZIS, SFO, and SFO/ZIS heterojunctions, the as-prepared samples were characterized by transmission electron microscopy (TEM). As shown in Figs. 4(a) and 4(b), ZIS and SFO show a flower-like microsphere and a nanoparticle morphology, respectively, which are consistent with the SEM results. As for 5% SFO/ZIS (Figs. 4(c) and 4(d)), the ZIS nanosheets attached by the SFO nanoparticles with an intimate interface can be observed, which facilitates the transfer of photogenerated charges, thereby further increasing the rate of the photocatalytic reactions [37]. Furthermore, lattice fringes with lattice distances (*d*) of 0.32 and 0.29 nm can be well labeled to the (102) crystal plane of ZIS and the (220) crystal plane of SFO, respectively,

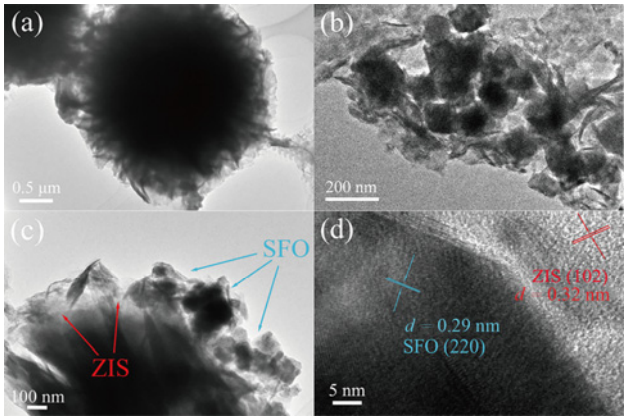

Fig. 4 TEM images of (a) pure ZIS, (b) SFO, and (c, d) 5% SFO/ZIS.

which indicates the successful construction of the SFO/ZIS heterojunction with an intimate interface.

To explore surface elemental chemical compositions and bonding states in the as-prepared samples, an X-ray photoelectron spectroscopy (XPS) measurement was employed, in which the C 1s standard peak (284.8 eV) was used as a reference to calibrate binding energies. In the survey spectra (Fig. 5(a)), all samples consist of the expected elements. High-resolution XPS spectra of the expected elements in the samples are compared in Figs. 5(b)–5(h). As can be seen in the F 1s spectra (Fig. 5(b)), one characteristic peak at 687.9 eV can be observed, corresponding to F^- in PVDF [27]. For ZIS, the XPS peaks at 1021.8 and 1044.8 eV are in accord with Zn $2p_{3/2}$ and Zn $2p_{1/2}$ of Zn^{2+}, respectively, indicating that Zn exists as Zn^{2+} in ZIS (Fig. 5(c)) [38]. For the In 3d spectra of ZIS (Fig. 5(d)), the two characteristic peaks at 444.8 and 452.4 eV are indexed to the In $3d_{5/2}$ and In $3d_{3/2}$ spin orbits, respectively, attributing to In^{3+} in ZIS [39]. Moreover, the XPS spectra of S 2p can be fitted into two contributions: The binding energies at 161.5 and 162.6 eV can be assigned to S $2p_{3/2}$ and S $2p_{1/2}$, respectively. In 5% SFO/ZIS, two similar peaks of the binding energies at 161.4 and 162.6 eV can be observed, as exhibited in Fig. 5(e) [40]. Additionally, the Sn 3d spectrum of SFO (Fig. 5(f)) exhibits two characteristic peaks at 485.8 and 494.2 eV, which belong to Sn $3d_{5/2}$ and Sn $3d_{3/2}$, respectively [15,16]. The Fe 2p spectra in SFO (Fig. 5(g)) can be divided into Fe $2p_{3/2}$ and Fe $2p_{1/2}$ (710.7 and 724.4 eV, respectively) with two broad satellite peaks at 715.9 and 732.5 eV, respectively. The clear satellite peaks indicate the high-spin Fe^{3+} valence state of Fe in SFO [15,41]. The O 1s region of SFO (Fig. 5(h)) can be split into two peaks at 530.3 and 531.5 eV, corresponding to the lattice oxygen of SFO and the surface absorbed oxygen, respectively [42]. Surprisingly, P–5% SZ films only present a higher energy peak at approximate 531.6 eV for O 1s, which is usually attributed to surface-absorbed oxygen species [43,44]. With respect to 5% SFO/ZIS, the related Zn $2p_{3/2}$ (1021.6 eV) and Zn $2p_{1/2}$ (1044.6 eV) peaks shift to lower binding energies, and a similar change trend is also observed in the In $3d_{5/2}$ (444.6 eV) and In $3d_{3/2}$ (452.2 eV) peaks, demonstrating increase electron density in ZIS after hybridizing with SFO. Inversely, the Sn $3d_{5/2}$ (485.9 eV) and Sn $3d_{3/2}$ (494.3 eV)) peaks in 5% SFO/ZIS show a slight positive shift of 0.1 eV compared with those of SFO, suggesting the decreased electron density of SFO in 5% SFO/ZIS. The changes in the binding energies for 5% SFO/ZIS demonstrate the strong electronic interaction between SFO and ZIS, which builds a mediator bridge for the electron transfer from SFO to ZIS [9]. Noticeably, compared with the peaks of SFO and ZIS mentioned above, the peaks of all elements in the P–5% SZ films exhibit a positive or negative shift, which can be attributed to the charges exchange between F ions and metal ions, thereby indicating that the interfaces between three monomers are tight [11,45]. Along with the TEM and elemental mapping results, the above XPS results provide convincing evidence that the SFO and ZIS particles are exposed on the surface of the P–5% SZ film, thereby further demonstrating the successful construction of the P–5% SZ film piezophotocatalyst.

3.2 Optical property analysis

Ultraviolet–visible (UV–Vis) diffuse reflectance spectra (DRS) were recorded to evaluate visible light absorption properties of the as-prepared samples. As observed in Fig. 6(a), due to the narrow bandgap of the pristine SFO, the absorption curve of SFO displays intense absorption capability from UV to the visible light range (terminating at approximately 760 nm in the near-infrared region) [34]. In the case of bare ZIS, an intense absorption with a steep absorption edge at about 569 nm can be observed [46]. In addition, the pure PVDF films have no absorption in the visible light region, which means that the PVDF films could not generate photo-induced e^-–h^+ pairs under visible light irradiation [27]. After the SFO particles were loaded on the surface of the ZIS microspheres, the absorption edge of 5% SFO/ZIS exhibits a conspicuous

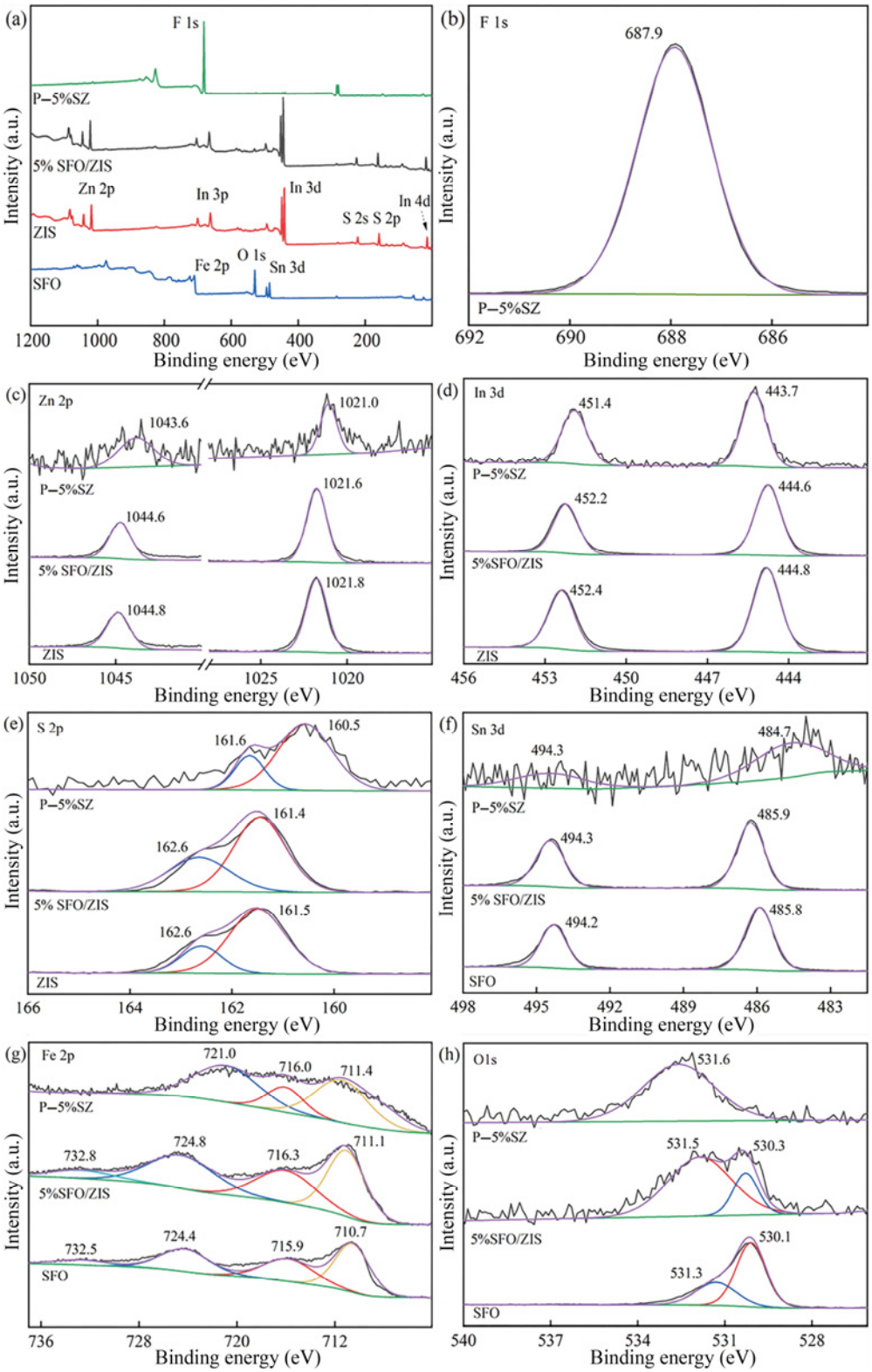

Fig. 5 (a) Survey XPS spectra and (b–h) high-resolution XPS spectra of F 1s, Zn 2p, In 3d, S 2p, Sn 3d, Fe 2p, and O 1s of ZIS, SFO, 5% SFO/ZIS, and P–5% SZ film.

red shift toward the higher-wavelength region compared to that of ZIS. This condition derives from the synergistic effect of SFO and ZIS [15]. Furthermore, the bandgap energy values (E_g) can be determined via Tauc plots of $(Ahv)^2$ ("A" represents the absorbance, and v represents the frequency) vs. hv [47], as can be

seen in Fig. 6(b). The E_g of bare ZIS, bare SFO, 5% SFO/ZIS, PVDF, and P–5% SZ films are 2.50, 1.85, 2.45, 5.16, and 2.36 eV, respectively.

3. 3 Piezoelectric characterization

Ferroelectric nature of the as-prepared P–5% SZ film piezophotocatalyst was directly unveiled by piezo-response force microscopy (PFM) with a conductive tip. PFM amplitude and phase images of the P–5% SZ films are presented in Figs. 7(a) and 7(c), respectively. From the PFM amplitude images, a clear region of chiaroscuro can be seen, which indicates the presence of randomly distributed upward and downward polarization domains [48]. Simultaneously, the strong phase contrast in the PFM phase image also represents different polarization directions and intensity [49]. To further investigate the local piezo-response of the P–5% SZ film samples, the amplitude–voltage curve and phase hysteresis loop were measured under the scanning of the applied direct current (DC) bias voltage, as shown in Figs. 7(b) and 7(d), respectively. The amplitude change of the piezoelectric response signal is diametrically correlated with local strain of the film. Also, this amplitude vs. voltage curve resembles a typical butterfly ring shape, which is a recognized property of ferroelectric materials [50].

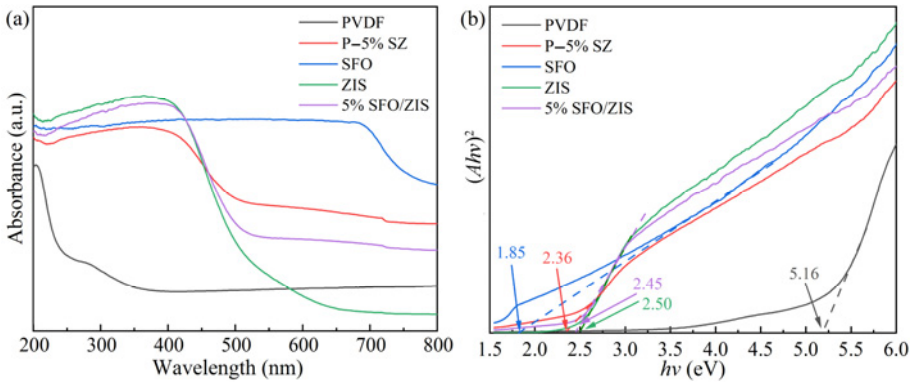

Fig. 6 (a) UV–Vis DRS spectra and (b) bandgaps of SFO, ZIS, 5% SFO/ZIS, PVDF, and P–5% SZ films.

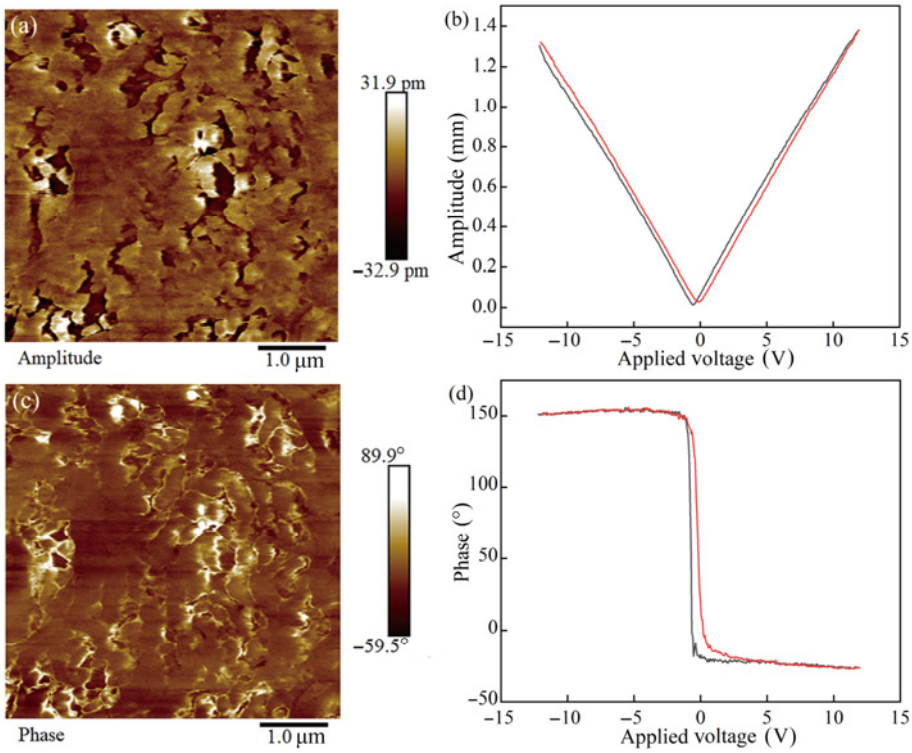

Fig. 7 Piezoelectric characterizations of P–5% SZ film: (a) amplitude image, (b) amplitude–voltage loop, (c) phase image, and (d) phase–voltage hysteresis loop.

From the phase hysteresis loop, an abrupt phase shifts from −27° to 153° as the reversal field shifts from +12 to −12 V, respectively, implying the occurrence of 180° domains and distinct polarization response switching behaviors in the P–5% SZ film [51]. Also, both the butterfly and phase hysteresis loops are horizontally shifted, and the polarization is reversible, which can be attributed to the presence of the internal bias field inside the films. The above results demonstrate that the P–5% SZ film piezophotocatalyst has excellent piezoelectric characteristics.

To directly investigate the potential output of the prepared P–5% SZ film piezophotocatalyst, copper sheets were attached to both sides of the film, and a constant pressure was applied to the films with certain *v* via a homemade instrument. The piezoelectric potential output signal on the film was then recorded by an oscilloscope (TBS1154, Teck Technology Co., Ltd., China), as shown in Fig. 8. In the absence of any pressure, no potential signal was recorded, because the adjacent negative charges to each other within the film cancelled out positive charges, making it electrically neutral overall. In contrast, under the periodically applied forces, localized polarized charges were generated on the surface of the P–5% SZ film, thereby forming piezoelectric potential [52]. These results show that the P–5% SZ film has appreciable

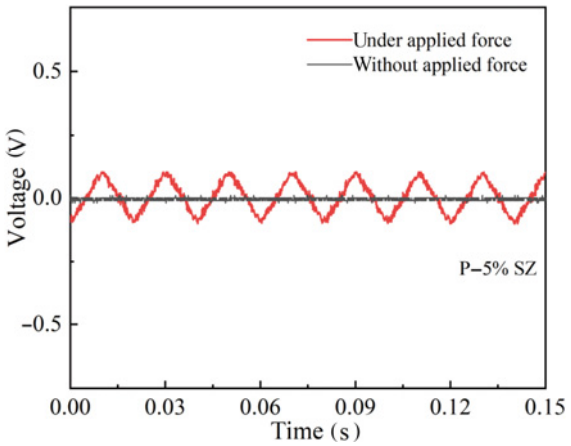

Fig. 8 Piezoelectric potential output signals over P–5% SZ film.

piezoelectric properties, and the film is quite sensitive to the action of external forces. In addition, it can be reasonably inferred that the P–5% SZ film piezophotocatalyst can absorb the energy of ambient vibration to generate the piezoelectric potential.

3. 4 Piezophotocatalytic H_2 evolution properties

Piezophotocatalytic hydrogen generation performance of the as-prepared heterojunction and film piezophotocatalysts are presented in Fig. S1 in the ESM and Figs. 9(a) and 9(b), respectively. Apparently,

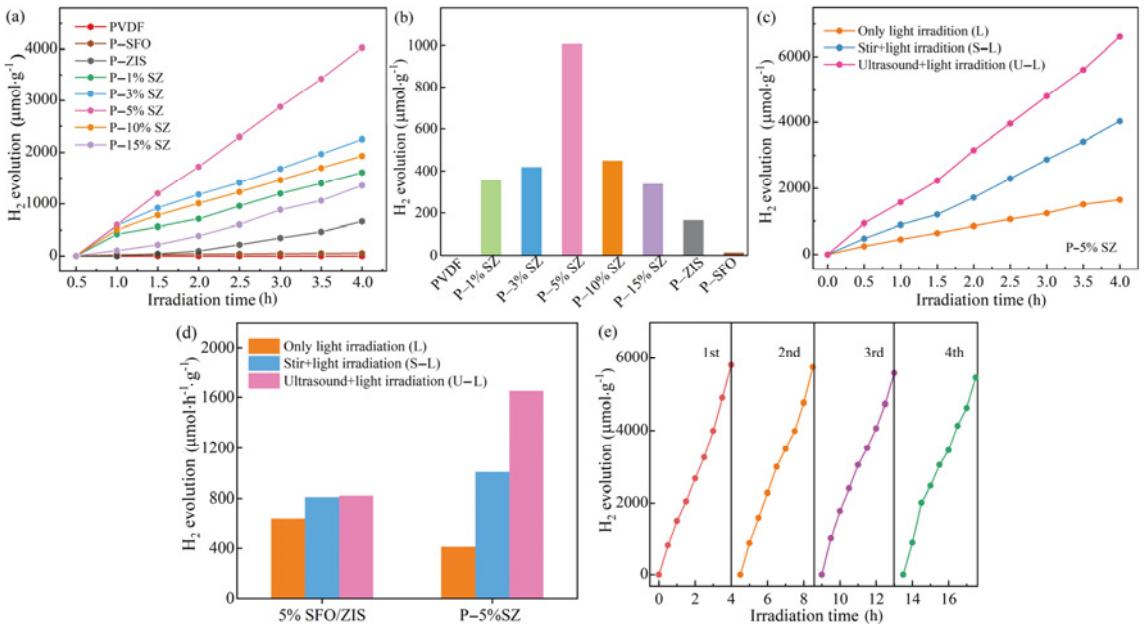

Fig. 9 (a) Time-dependent photocatalytic H_2 generation rates and (b) average photocatalytic H_2 generation rates of as-obtained P–SZ films under S–L. (c) Comparison of H_2 generation performance within 4 h over the as-synthesized P–5% SZ film under three conditions (L, S–L, and U–L). (d) Comparison of H_2 generation rates by 5% SFO/ZIS and P–5% SZ film under three different conditions. (e) Cyclic stabilities over P–5% SZ films under U–L. Note: L, S–L, and U–L represent light irradiation, stirring and light irradiation, and both ultrasonic wave vibration and light irradiation, respectively.

the pristine PVDF exhibits no H_2 production, and other samples exhibit linearly increasing hydrogen evolution amounts with the increasing irradiation time. As displayed in Fig. S1 in the ESM, ZIS displays a hydrogen evolution rate of 235.21 μmol·h^{-1}·g^{-1}, whereas SFO has the minimal generation of H_2 with a yield of 11.5 μmol·h^{-1}·g^{-1} [41]. By comparing the performance of ZIS and SFO/ZIS heterojunctions, the hydrogen production rate of SFO/ZIS is generally higher than that of pure ZIS, and the hydrogen production rate of 5% SFO/ZIS is about 846.79 μmol·h^{-1}·g^{-1}, which is 3.6 times that of ZIS. The reason for this phenomenon is that the photogenerated carrier separation was promoted by the formed heterojunction between SFO and ZIS. This further demonstrates that the existence of the SFO/ZIS heterojunction can boost the photocatalytic activity of the P–SZ film. Furthermore, the P–SZ film shows better photocatalytic activity than P–ZIS and P–SFO, which is in line with expectation. With the increase of the SFO content, the photocatalytic hydrogen evolution rate of P–SZ firstly increased, and then decreased. When x of SFO to ZIS is 5%, the film shows the largest hydrogen evolution rate of 1007.3 μmol·h^{-1}·g^{-1}, which exceeds that of the P–ZIS films by an approximate factor of 8.43. However, superfluous SFO particles loading on the ZIS microspheres can reduce the photocatalytic performance of the P–SZ films, due to the reduced active sites and blocked absorption of visible light [53]. AQEs of the P–5% SZ film exposed to light irradiation at different monochromatic wavelengths are calculated and displayed in Fig. S3 in the ESM.

To investigate the influence of the piezoelectric field generated by the PVDF film, the H_2 production performance for the P–5% SZ piezophotocatalyst were further tested under three different conditions of only L, S–L, and U–L (the ultrasonic vibration is 40 kHz, and the power is 50 W). As depicted in Figs. 9(c) and 9(d), the ratio among conditions of L (412.0 μmol·h^{-1}·g^{-1}), S–L (1007.3 μmol·h^{-1}·g^{-1}), and U–L (1652.7 μmol·h^{-1}·g^{-1}) is 1 : 2.4 : 4.0. Apparently, the hydrogen evolution rate under the L condition is the lowest, which can be attributed to no mechanical bending to generate the piezoelectric field. However, when the ultrasonic wave was applied, the bending of the P–SZ film was more intense, leading to the strongest piezoelectric field, and thus the highest photoactivity was achieved [45]. This was further proved by a photocatalytic time-dependent hydrogen evolution curve of the P–5% SZ films under an interval L/(U–L) condition, as shown in Fig. S4 in the ESM. Apparently, the slope of the curve is low under the L condition, and the slope increases significantly when ultrasound was applied. These results confirm that the as-prepared PVDF-based film piezophotocatalyst can be motivated by ultrasonic waves to generate a piezoelectric field to promote the separation of the photogenerated carriers, and thus achieve enhanced photoactivity.

It is well known that both stirring and ultrasonic vibration can promote the diffusion of reactants and accelerate the desorption of H_2 from the surface of the photocatalysts, thereby leading to the improvement of the photocatalytic performance to some extent. To differentiate the role of the piezoelectric effect in the photoreaction, we compared the enhancement ratio in the photocatalytic activity of the P–5% SZ film (with the piezoelectric effect) and the 5% SFO/ZIS powders (without the piezoelectric effect) under three different conditions (L, S–L, and U–L), as depicted in Fig. 9(d). Obviously, the hydrogen production rates of 5% SFO/ZIS under the S–L and U–L conditions are almost comparable and increased by factors of 1.27 and 1.29 times, respectively, in comparison with that under the L condition. Apparently, the enhancement of the boosted mass transfer process due to stirring and sonication is slight, whose enhancement ratios can be estimated to be 0.27 and 0.29, respectively. Comparatively, in comparison with that under the L condition, the photoactivity of the P–5% SZ film was significantly improved by 2.44 and 4.01 times under the S–L and U–L conditions, respectively, which are much higher than that of 5% SFO/ZIS. This means that there is another contributing factor in addition to the above-mentioned boosting mass transfer process. As discussed in Section 3.3, it is reasonable to deduce that the piezoelectric effect of PVDF caused by the vibration played key roles in the photocatalytic hydrogen production under the S–L and U–L conditions. Both water stirring and ultrasonic waves excite PVDF to generate piezoelectric fields, which provide a driving force for efficient carrier separation. The enhancement ratios of three effects of piezoelectricity, improved mass transfer, and heterojunction over the P–5% SZ film are presented in Fig. S5 in the ESM. Based on the enhancement ratios of 0.27 and 0.29 due to improved mass transfer under S–L and U–L of 5% SFO/ZIS, respectively, the enhancement ratios of the piezoelectric effect over P–5% SZ excited by water

stirring and ultrasonic waves can be estimated to be 2.17 and 3.72, respectively.

According to the above analysis, it is certain that (i) the constructed heterojunction between SFO and ZIS can result in the improved photocatalytic performance, which is beneficial to promoting charge separation; (ii) the photocatalytic activity can be further improved significantly by the piezoelectric effect, which has ability to utilize ambient vibration to provide the driving force for the separation of the charges.

As plotted in Fig. 9(e), it is evident that the H_2 evolution capacity of the P–5% SZ film piezophotocatalyst shows commendable stability with no distinct decrease under continuous illumination for four reaction cycles. In addition, the film can be collected and recovered directly from the reaction solution with remarkable reusability. Furthermore, the XRD and SEM results show no obvious phase structure or morphology alterations after the cycle test, as displayed in Figs. S6 and S7 in the ESM, respectively, can further demonstrate remarkable stability of the P–SZ films.

3. 5 Charge transfer and separation

To further understand the transfer and separation of interfacial photogenerated charges, photoluminescence (PL) spectra, transient photocurrent response, and electrochemical impedance spectroscopy (EIS) Nyquist plots of the samples were tested. As presented in Fig. 10(a), with an excitation wavelength of 390 nm, all samples show a distinct PL emission peak at approximately 509 nm [54]. Apparently, pure ZIS exhibits the highest PL emission peak intensity, which suggested that the migration and separation of the photogenerated charge carriers are inefficient [55]. Comparatively, after the formation of the heterojunction between SFO and ZIS, the PL intensity of 5% SFO/ZIS and P–5% SZ film are weaker, which means that the formed heterojunction significantly boosts the separation of the photogenerated carriers. The boosted charge separation was further confirmed by the higher photocurrent density of 5% SFO/ZIS and P–5% SZ film than that of ZIS, as shown in Fig. 10(b). Notably, under the U–L condition, the photocurrent of P–5% SZ was dramatically improved, which is in consistent with the above photocatalysis results. The piezoelectric field driven by ultrasonic vibration should be responsible for this, which can boost the charge generation and accelerate the separation of photoinduced charges [35]. As displayed in Fig. 10(c), Z' vs. $-Z''$ curves of the EIS Nyquist diagrams, in which the real and imaginary parts of the impedance at different frequencies are defined as Z' and Z'', respectively, were further studied to insight into the capability of the charge migrations [37]. The charge transfer resistances (R_{ct}) at the semiconductor–electrolyte interface was assessed from the arc radius of Nyquist plots. All these photoelectric measurements suggest that the formation of the heterojunction and the piezoelectric property of PVDF can boost the charge separation and speed up the charge transfer, consequently resulting in the improved photocatalytic H_2 evolution.

3. 6 Photocatalytic mechanism

Mott–Schottky (M–S) curves were recorded at different frequencies, as displayed in Figs. 11(a) and 11(b), to provide insight into the approximate electronic energy level structures of the SFO/ZIS heterojunction. It is noted that both linear parts of the M–S curves for SFO and ZIS have positive slopes, which demonstrates that SFO and ZIS belong to n-type semiconductors. This is matched with those reported in Refs. [15,37]. Furthermore, the flat band potential of SFO and ZIS can be roughly estimated by extrapolating the linear section of the M–S plots to $1/C^2 = 0$ and are −0.72 and −0.64 V (vs. saturated calomel electrode (SCE)), respectively [56]. Meanwhile, the Fermi level (E_f) values of SFO and ZIS are about −0.48 and −0.40 V

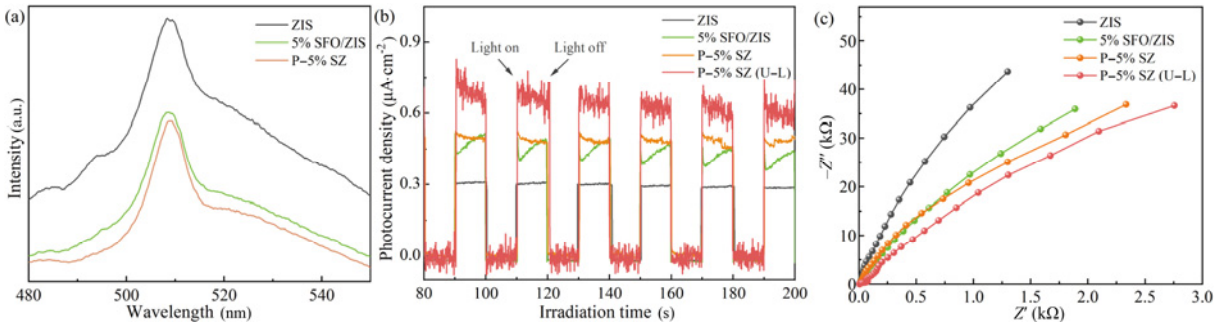

Fig. 10 (a) PL spectra, (b) transient photocurrent response, and (c) EIS Nyquist plots of samples.

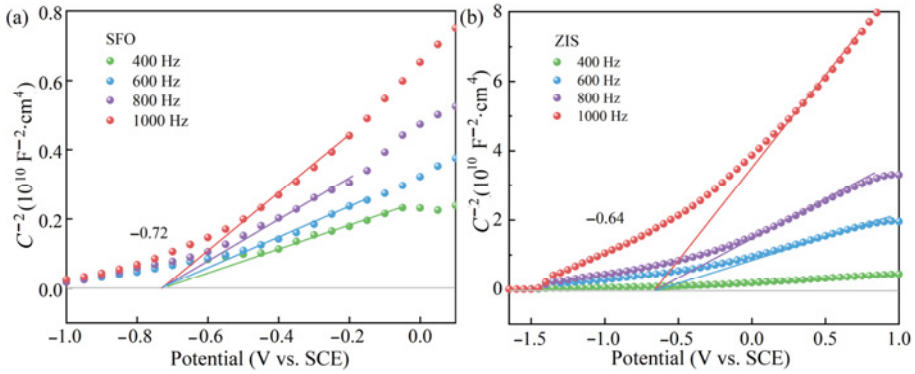

Fig. 11 M–S curves of (a) SFO and (b) ZIS.

(vs. normal hydrogen electrode (NHE)), respectively, as obtained by the Nernst equation between SCE and NHE: $E_{NHE} = E_{SCE} + 0.242$, in which E_{NHE} and E_{SCE} are defined as the potential of the normal hydrogen electrode and the potential of the saturated calomel electrode, respectively [57]. The conduction band levels (E_{CB}) of SFO and ZIS were calculated as −0.68 and −0.59 V, respectively, since E_{CB} is generally 0.2 V negative than the E_f value for most n-type semiconductors. Meanwhile, the E_g values of SFO and ZIS are 1.85 and 2.50 eV from DRS results, respectively, as represented in Fig. 5(b). Therefore, the valence band levels (E_{VB}) of SFO and ZIS are located at 1.17 and 1.91 V, respectively, combined with the following equation [6]: $E_{VB} = E_{CB} + E_g$.

Under visible light excitation, electron paramagnetic resonance (EPR) measurements were carried out to determine photocatalytic active species during the photocatalytic reaction, using 5,5-dimethyl-1-pyrroline-N-oxide (DMPO) to trap •OH and $•O_2^-$. As shown in Fig. 12(a), four characteristic peaks attributed to DMPO–$•O_2^-$ radicals can be observed over SFO and ZIS, which may thank their more negative CB potential (−0.68 and −0.59 V vs. NHE, respectively) in comparison with the standard reduction potential of $O_2/•O_2^-$ (−0.33 V vs. NHE) [58]. As presented in Fig. 12(b), the featured signals of DMPO–•OH with an intensity ratio of 1 : 2 : 2 : 1 can be hardly observed over pristine SFO, due to that the band edge position of E_{VB} in SFO (1.17 V vs. NHE) is more negative than that of the standard $•OH/OH^-$ redox potential (1.90 V vs. NHE) [58]. Simultaneously, since E_{VB} (1.91 V vs. NHE) in ZIS is close to the standard $•OH/OH^-$ redox potential, only a slight DMPO–•OH characteristic peak can be observed on the pure ZIS, indicating that the small amount of •OH radicals were generated on the surface of the ZIS samples. It can be deduced that few •OH radicals were likely produced from multistep reduction of O_2 at the conduction band rather than the reaction of H_2O with holes at the valence band ($O_2 + e^- \rightarrow •O_2^-$, $•O_2^- + e^- + 2H^+ \rightarrow H_2O_2$, and $H_2O_2 + e^- \rightarrow •OH + OH^-$) [59]. It is worth noting that the 5% SFO/ZIS composite photocatalyst was unable to generate •OH radicals, and the $•O_2^-$ radical signal intensity was not significantly enhanced. In this regard, it is assumed that SFO and ZIS are constructed as a type II heterojunction structure [60]. Under visible light excitation, electrons on the conduction band of SFO are transferred to the conduction band of ZIS while holes migrate from the valence band of ZIS to the valence band of SFO.

With respect to the photocatalytic H_2 evolution, because of vacuum environment, the photogenerated electrons are mainly to reduce H^+ to produce H_2 instead of the reduction reaction with O_2. At the same time, the photogenerated holes are mainly consumed by sacrificial reagents such as methanol solution and Na_2S and Na_2SO_3 solution. To further prove the predominant role of electron radicals, the methanol solution was used instead of the Na_2S and Na_2SO_3 solution as hole trapping agent, and $AgNO_3$ (1 mmol, scavenger for e^-) was used to perform the hydrogen production experiment. As presented in Fig. S8 in the ESM, under the condition of ultrasound and illumination, the photocatalytic hydrogen production rates of 5% SFO/ZIS and P–5% SZ are both still 0 μmol·h^{-1}·g^{-1} after 4 h, suggesting that the addition of $AgNO_3$ significantly suppressed the photocatalytic activity of the catalysts, and the electrons played a dominant role in the photocatalytic hydrogen evolution reaction.

Based on the above experimental results, a plausible photocatalytic reaction mechanism based on the synergetic effects of the heterojunction and piezoelectricity for the enhanced H_2 generation of the P–SZ film piezophotocatalyst was further inferred, as displayed in Fig. 13. Firstly, a staggered type II

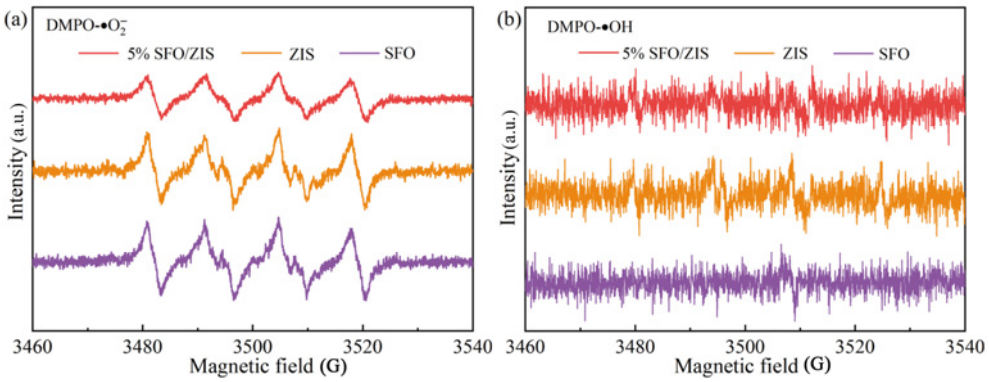

Fig. 12 EPR spectra of (a) DMPO–O_2^- and (b) DMPO–•OH for SFO, ZIS and 5% SFO/ZIS.

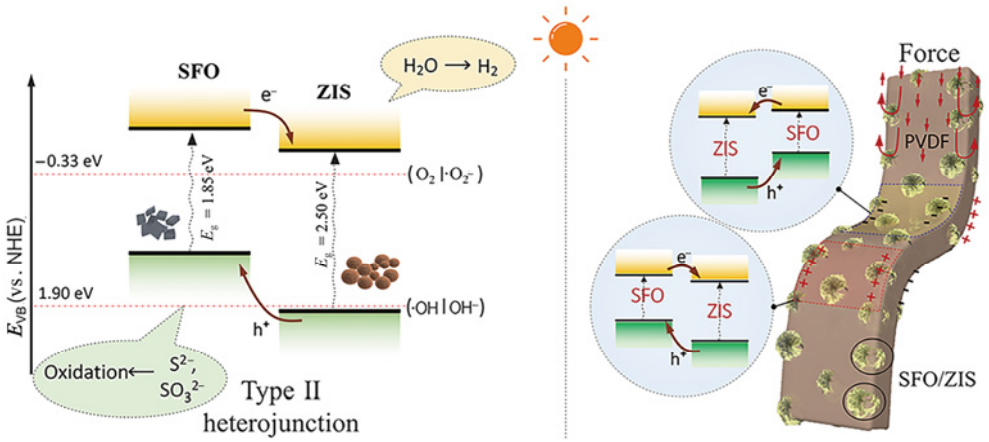

Fig. 13 Schematic diagram of improved photocatalytic H_2 evolution for P–SZ piezophotocatalyst.

heterojunction is formed after the close contact between SFO and ZIS. Under the excitation of visible light, both SFO and ZIS are excited simultaneously to generate e^- in CB, leaving behind h^+ in their VB. The diffusion of carriers occurs because of their different CB and VB potential, that is, e^- transfers from CB of SFO to that of ZIS, and meanwhile h^+ in the opposite direction, resulting in the boosted charge separation. Finally, the electrons in CB of ZIS can efficiently reduce H^+ to H_2 because E_{CB} of ZIS is more negative than the standard reduction potential of H^+/H_2, while the holes in VB of SFO are consumed by the sacrificial agent (S^{2-} and SO_3^{2-}). Secondly, along with the heterojunction effect, the piezoelectricity effect from the piezoelectric of PVDF will further boost the separation of photoinduced charges. Under the drive of the vibration caused by mechanical stirring or ultrasound, the bending of the P–SZ film takes place, which will generate positive or negative piezoelectric potential at the bending in the opposite direction, respectively. Apparently, under the influence of the piezoelectric potential, the photo-generated electrons and holes at the interface of the SFO/ZIS heterojunction are driven to diffuse in the opposite direction, thereby accelerating the transfer and separation of charges. When the migration direction of carriers driven by the piezoelectric field is consistent with the direction of charge diffusion by the effect of the heterojunction at the interface of the 5% SFO/ZIS heterojunction, it is more beneficial to promoting the carrier separation and accelerating the process of redox reaction. Admittedly, the opposite can happen. Fortunately, since the bending direction of the film photocatalyst is due to random or periodic vibration, the direction of the piezoelectric potential is constantly changing. Consequently, the probability of the carrier diffusion from two effects in the same direction is greatly increased, and thus the synergistic effect of the heterojunction and piezoelectricity can effectively enhance the photocatalytic hydrogen evolution performance.

4 Conclusions

In summary, this work constructed an efficient flexible P–SZ piezophotocatalytic film by coupling PVDF with

excellent piezoelectric propertiesand SFO/ZIS heterojunction. The P–5% SZ piezophotocatalyst exhibits the best hydrogen evolution rates of 1007.3 and 1652.7 $\mu mol \cdot h^{-1} \cdot g^{-1}$ under S–L and U–L, respectively, which are 2.44 and 4.01 times that under the L condition, respectively. This suggests the impressive capability of harvesting mechanical energy and solar energy. PFM and piezoelectric potential output results confirm the piezoelectricity of the P–SZ film. Moreover, the experimental results prove that the SFO/ZIS heterojunction was formed after their contact. Consequently, it is reasonable to infer that the improved piezophotocatalyst can be ascribed to the synergetic effects of the piezoelectricity and heterojunction, leading to the accelerated carrier transfer and the boosted charge separation at the interface of the SFO/ZIS heterojunction. In addition, the as-synthesized P–SZ piezophotocatalyst can not only harvest and utilize ambient mechanical energy, but also exhibit excellent recoverability and stability, showing great potential in the future energy and environmental fields.

Acknowledgements

This work was supported by Shandong Provincial Natural Science Foundation, China (Nos. ZR2021ME046 and ZR2022ME179) and Liaocheng University College Students Innovation and Entrepreneurship Training Program (No. 2020205926).

Declaration of competing interest

The authors have no competing interests to declare that are relevant to the content of this article.

Electronic Supplementary Material

Supplementary material is available in the online version of this article at https://doi.org/10.26599/JAC.2023.9220758.

References

[1] Hisatomi T, Domen K. Reaction systems for solar hydrogen production via water splitting with particulate semiconductor photocatalysts. *Nat Catal* 2019, **2**: 387–399.

[2] Lu Y, Li Y, Wang YY, *et al*. Two-photon induced NIR active core–shell structured WO_3/CdS for enhanced solar light photocatalytic performance. *Appl Catal B-Environ* 2020, **272**: 118979.

[3] Tian N, Hu C, Wang JJ, *et al*. Layered bismuth-based photocatalysts. *Coordin Chem Rev* 2022, **463**: 214515.

[4] Fan GD, Cai CJ, Chen ZY, *et al*. Visible-light-drivenself-floating Ag_2MoO_4/TACN@LF photocatalyst inactivation of *Microcystis aeruginosa*: Performance and mechanisms. *J Hazard Mater* 2023, **441**: 129932.

[5] Jiang JZ, Li FY, Xiong ZG, *et al*. Two-dimensional modified carbon-based materials for efficient photocatalytic hydrogen production. *J Liaocheng Univ* (*Nat Sci Ed*) 2023, **36**: 73–84. (in Chinese)

[6] Geng YL, Zou XL, Lu YA, *et al*. Fabrication of the SnS_2/$ZnIn_2S_4$ heterojunction for highly efficient visible light photocatalytic H_2 evolution. *Int J Hydrogen Energ* 2022, **47**: 11520–11527.

[7] Yuan RR, Qiu JL, Yue CL, *et al*. Self-assembled hierarchical and bifunctional MIL-88A(Fe)@$ZnIn_2S_4$ heterostructure as a reusable sunlight-driven photocatalyst for highly efficient water purification. *Chem Eng J* 2020, **401**: 126020.

[8] Li Y, Li Z, Liu EZ. Preparation of $NiMoO_4$/$ZnIn_2S_4$ S-scheme heterojunctions and enhancement mechanism of photocatalytic hydrogen production. *J Liaocheng Univ* (*Nat Sci Ed*) 2023, **36**: 1–10. (in Chinese)

[9] Li CX, Che HN, Yan YS, *et al*. Z-scheme $AgVO_3$/$ZnIn_2S_4$ photocatalysts: “One Stone and Two Birds” strategy to solve photocorrosion and improve the photocatalytic activity and stability. *Chem Eng J* 2020, **398**: 125523.

[10] Yang WL, Zhang L, Xie JF, *et al*. Enhanced photoexcited carrier separation in oxygen-doped $ZnIn_2S_4$ nanosheets for hydrogen evolution. *Angew Chem Int Ed* 2016, **55**: 6716–6720.

[11] Kong DZ, Yin D, Zhang DF, *et al*. Noble metal-free 0D–1D NiCoP/$Mn_{0.3}Cd_{0.7}S$ nanocomposites for highly efficient photocatalytic H_2 evolution under visible-light irradiation. *Nanotechnology* 2020, **31**: 305701.

[12] Li FY, Jiang J, Li N, *et al*. Design and fabrication of hollow structured Cu_2MoS_4/$ZnIn_2S_4$ nanocubes with significant enhanced photocatalytic hydrogen evolution performance. *Int J Hydrogen Energ* 2021, **46**: 37847–37859.

[13] Wang XL, Li YY, Li ZH. Efficient visible light initiated hydrothiolations of alkenes/alkynes over Ir_2S_3/$ZnIn_2S_4$: Role of Ir_2S_3. *Chinese J Catal* 2021, **42**: 409–416.

[14] Yang HC, Cao RY, Sun PX, *et al*. Constructing electrostatic self-assembled 2D/2D ultra-thin $ZnIn_2S_4$/protonated g-C_3N_4 heterojunctions for excellent photocatalytic performance under visible light. *Appl Catal B-Environ* 2019, **256**: 117862.

[15] Wang J, Zhang Q, Deng F, *et al*. Rapid toxicity elimination of organic pollutants by the photocatalysis of environment-friendly and magnetically recoverable step-scheme $SnFe_2O_4$/$ZnFe_2O_4$ nano-heterojunctions. *Chem Eng J* 2020, **379**: 122264.

[16] Jia YF, Wang QZ, Zhang WB, *et al*. Octahedron-shaped $SnFe_2O_4$ for boosting photocatalytic degradation and CO_2 reduction. *J Alloys Compd* 2021, **889**: 161737.

[17] Kong DZ, Fan HH, Yin D, *et al*. $AgFeO_2$ nanoparticle/$ZnIn_2S_4$ microsphere p–n heterojunctions with hierarchical

nanostructures for efficient visible-light-driven H_2 evolution. *ACS Sustainable Chem Eng* 2021, **9**: 2673–2683.

[18] Jia YF, Zhang WB, Do JY, *et al*. Z-scheme $SnFe_2O_4$/α-Fe_2O_3 micro-octahedron with intimated interface for photocatalytic CO_2 reduction. *Chem Eng J* 2020, **402**: 126193.

[19] Wu T, Liang QH, Tang L, *et al*. Construction of a novel S-scheme heterojunction piezoelectric photocatalyst V-$BiOIO_3$/FTCN and immobilization with floatability for tetracycline degradation. *J Hazard Mater* 2023, **443**: 130251.

[20] Ren ZR, Chen F, Zhao Q, *et al*. Efficient CO_2 reduction to reveal the piezocatalytic mechanism: From displacement current to active sites. *Appl Catal B-Environ* 2023, **320**: 122007.

[21] Kumar A, Krishnan V. Vacancy engineering in semiconductor photocatalysts: Implications in hydrogen evolution and nitrogen fixation applications. *Adv Funct Mater* 2021, **31**: 2009807.

[22] Wang PL, Li XY, Fan SY, *et al*. Impact of oxygen vacancy occupancy on piezo-catalytic activity of $BaTiO_3$ nanobelt. *Appl Catal B-Environ* 2020, **279**: 119340.

[23] Zhang DF, Su CH, Li H, *et al*. Synthesis and enhanced piezophotocatalytic activity of Ag_2O/$K_{0.5}Na_{0.5}NbO_3$ composites. *J Phys Chem Solids* 2020, **139**: 109326.

[24] Zhao ZL, Zhou J, Shu Z. Efficient piezo-catalytic oxidation of aqueous As(III) over crystalline carbon nitride poly(heptazine imide). *Chem Eng J* 2022, **449**: 137868.

[25] Li S, Zhao ZC, Yu DF, *et al*. Few-layer transition metal dichalcogenides (MoS_2, WS_2, and WSe_2) for water splitting and degradation of organic pollutants: Understanding the piezocatalytic effect. *Nano Energy* 2019, **66**: 104083.

[26] Kim YS, Xie YN, Wen XN, *et al*. Highly porous piezoelectric PVDF membrane as effective lithium ion transfer channels for enhanced self-charging power cell. *Nano Energy* 2015, **14**: 77–86.

[27] Zhang DF, Liu XH, Wang SC, *et al*. Enhanced charges separation to improve hydrogen production efficiency by organic piezoelectric film polarization. *J Alloys Compd* 2021, **869**: 159390.

[28] Dai BY, Huang HM, Wang FL, *et al*. Flowing water enabled piezoelectric potential of flexible composite film for enhanced photocatalytic performance. *Chem Eng J* 2018, **347**: 263–272.

[29] Wan LC, Tian WR, Li NJ, *et al*. Hydrophilic porous PVDF membrane embedded with $BaTiO_3$ featuring controlled oxygen vacancies for piezocatalytic water cleaning. *Nano Energy* 2022, **94**: 106930.

[30] Yin X, Wu W, Zhang FS, *et al*. Synergetic effect of piezoelectricity and heterojunction on photocatalytic performance. *J Photoch Photobio A* 2020, **400**: 112661.

[31] Shao ZW, Meng X, Lai H, *et al*. Coralline-like Ni_2P decorated novel tetrapod-bundle $Cd_{0.9}Zn_{0.1}S$ ZB/WZ homojunctions for highly efficient visible-light photocatalytic hydrogen evolution. *Chinese J Catal* 2021, **42**: 439–449.

[32] Liu H, Zhang J, Ao D. Construction of heterostructured $ZnIn_2S_4$@NH_2–MIL-125(Ti) nanocomposites for visible-light-driven H_2 production. *Appl Catal B-Environ* 2018, **221**: 433–442.

[33] Guan DC, Tian S, Sun YH, *et al*. Investigation of the electrochemical properties and kinetics of a novel $SnFe_2O_4$@nitrogen-doped carbon composite anode for lithium-ion batteries. *Electrochim Acta* 2019, **322**: 134722.

[34] Jiang X, Wang MT, Luo BN, *et al*. Magnetically recoverable flower-like Sn_3O_4/$SnFe_2O_4$ as a type-II heterojunction photocatalyst for efficient degradation of ciprofloxacin. *J Alloys Compd* 2022, **926**: 166878.

[35] Li M, Sun JX, Chen G, *et al*. Construction double electric field of sulphur vacancies as medium ZnS/Bi_2S_3–PVDF self-supported recoverable piezoelectric film photocatalyst for enhanced photocatalytic performance. *Appl Catal B-Environ* 2022, **301**: 120792.

[36] Kong DZ, Ruan XX, Geng JK, *et al*. 0D/3D $ZnIn_2S_4$/$Ag_6Si_2O_7$ nanocomposite with direct Z-scheme heterojunction for efficient photocatalytic H_2 evolution under visible light. *Int J Hydrogen Energ* 2021, **46**: 28043–28052.

[37] Kong DZ, Hu XC, Geng JK, *et al*. Growing $ZnIn_2S_4$ nanosheets on $FeWO_4$ flowers with p–n heterojunction structure for efficient photocatalytic H_2 production. *Appl Surf Sci* 2022, **591**: 153256.

[38] Tao JN, Wang MY, Liu GW, *et al*. Efficient photocatalytic hydrogen evolution coupled with benzaldehyde production over 0D $Cd_{0.5}Zn_{0.5}S$/2D Ti_3C_2 Schottky heterojunction. *J Adv Ceram* 2022, **11**: 1117–1130.

[39] Wang SB, Guan BY, Lou XW. Construction of $ZnIn_2S_4$–In_2O_3 hierarchical tubular heterostructures for efficient CO_2 photoreduction. *J Am Chem Soc* 2018, **140**: 5037–5040.

[40] Gao ZQ, Chen KY, Wang L, *et al*. Aminated flower-like $ZnIn_2S_4$ coupled with benzoic acid modified g-C_3N_4 nanosheets via covalent bonds for ameliorated photocatalytic hydrogen generation. *Appl Catal B-Environ* 2020, **268**: 118462.

[41] Jo WK, Moru S, Tonda S. Magnetically responsive $SnFe_2O_4$/g-C_3N_4 hybrid photocatalysts with remarkable visible-light-induced performance for degradation of environmentally hazardous substances and sustainable hydrogen production. *Appl Surf Sci* 2020, **506**: 144939.

[42] Xiao SH, Fakhri A, Janani BJ. Synthesis of spinel tin ferrite decorated on bismuth ferrite nanostructures for synergetic photocatalytic, superior drug delivery, and antibacterial efficiencies. *Surf Interfaces* 2021, **27**: 101490.

[43] Jia YF, Ma HX, Zhang WB, *et al*. Z-scheme $SnFe_2O_4$–graphitic carbon nitride: Reusable, magnetic catalysts for enhanced photocatalytic CO_2 reduction. *Chem Eng J* 2020, **383**: 123172.

[44] Zheng NC, Ouyang T, Chen YB, *et al*. Ultrathin CdS shell-sensitized hollow S-doped CeO_2 spheres for efficient visible-light photocatalysis. *Catal Sci Technol* 2019, **9**: 1357–1364.

[45] Han SW, Chen D, Wang J, *et al*. Assembling Sn_3O_4 nanostructures on a hydrophobic PVDF film through metal–F coordination to construct a piezotronic effect-

enhanced Sn_3O_4/PVDF hybrid photocatalyst. *Nano Energy* 2020, **72**: 104688.

[46] Chen JS, Xin F, Yin XH, *et al*. Synthesis of hexagonal and cubic $ZnIn_2S_4$ nanosheets for the photocatalytic reduction of CO_2 with methanol. *RSC Adv* 2015, **5**: 3833–3839.

[47] Wu J, Li LY, Li XA, *et al*. A novel 2D graphene oxide modified α-$AgVO_3$ nanorods: Design, fabrication, and enhanced visible-light photocatalytic performance. *J Adv Ceram* 2022, **11**: 308–320.

[48] He TF, Cao ZZ, Li GR, *et al*. High efficiently harvesting visible light and vibration energy in $(1-x)AgNbO_3$–$xLiTaO_3$ solid solution around antiferroelectric–ferroelectric phase boundary for dye degradation. *J Adv Ceram* 2022, **11**: 1641–1653.

[49] Tang Y, Chen XQ, Zhu MD, *et al*. The strong alternating built-in electric field sourced by ball milling on Pb_2BO_3X (X = Cl, Br, I) piezoelectric materials contributes to high catalytic activity. *Nano Energy* 2022, **101**: 107545.

[50] Wang F, Zhang JT, Jin CC, *et al.* Unveiling the effect of crystal facets on piezo-photocatalytic activity of $BiVO_4$. *Nano Energy* 2022, **101**: 107573.

[51] Wang PL, Fan SY, Li XY, *et al*. Piezotronic effect and hierarchical Z-scheme heterostructure stimulated photocatalytic H_2 evolution integrated with C–N coupling of benzylamine. *Nano Energy* 2021, **89**: 106349.

[52] You DT, Liu L, Yang ZY, *et al*. Polarization-induced internal electric field to manipulate piezo-photocatalytic and ferro-photoelectrochemical performance in bismuth ferrite nanofibers. *Nano Energy* 2022, **93**: 106852.

[53] Tang YX, Kong DZ, Wang XT, *et al*. Construction of direct Z-scheme system for enhanced visible light photocatalytic activity based on $Zn_{0.1}Cd_{0.9}S/FeWO_4$ heterojunction. *Nanotechnology* 2019, **30**: 475704.

[54] Qiu JH, Li M, Xu J, *et al*. Bismuth sulfide bridged hierarchical Bi_2S_3/BiOCl@$ZnIn_2S_4$ for efficient photocatalytic Cr(VI) reduction. *J Hazard Mater* 2020, **389**: 121858.

[55] Raja A, Son N, Kang M. Direct Z-scheme $ZnIn_2S_4$ spheres and CeO_2 nanorods decorated on reduced-graphene-oxide heterojunction photocatalysts for hydrogen evolution and photocatalytic degradation. *Appl Surf Sci* 2023, **607**: 155087.

[56] Su XL, Fan D, Sun HW, *et al*. One-dimensional rod-shaped $Ag_2Mo_2O_7$/BiOI n–n junctions for efficient photodegradation of tetracycline and rhodamine B under visible light. *J Alloys Compd* 2022, **912**: 165184.

[57] Yao XT, Zhen HR, Zhang DF, *et al*. Microwave-assisted hydrothermal synthesis of broadband Yb^{3+}/Er^{3+} co-doped BiOI/Bi_2O_4 photocatalysts with synergistic effects of upconversion and direct Z-scheme heterojunction. *Colloid Surface A* 2022, **648**: 129276.

[58] Zhao Y, Xu QQ, Zhou XF, *et al*. Enhanced photo-piezo-catalytic properties of Co-doped $Ba_{0.85}Ca_{0.15}Zr_{0.1}(Ti_{1-x}Co_x)_{0.9}$ ferroelectric ceramics for dye degradation. *Ceram Int* 2023, **49**: 8259–8270.

[59] Hu JD, Chen C, Zheng Y, *et al*. Spatially separating redox centers on Z-scheme $ZnIn_2S_4/BiVO_4$ hierarchical heterostructure for highly efficient photocatalytic hydrogen evolution. *Small* 2020, **16**: 2002988.

[60] Zhang M, Yao JC, Arif M, *et al*. 0D/2D $CeO_2/ZnIn_2S_4$ Z-scheme heterojunction for visible-light-driven photocatalytic H_2 evolution. *Appl Surf Sci* 2020, **526**: 145749.

Open Access This article is licensed under a Creative Commons Attribution 4.0 International License, which permits use, sharing, adaptation, distribution and reproduction in any medium or format, as long as you give appropriate credit to the original author(s) and the source, provide a link to the Creative Commons licence, and indicate if changes were made.

The images or other third party material in this article are included in the article's Creative Commons licence, unless indicated otherwise in a credit line to the material. If material is not included in the article's Creative Commons licence and your intended use is not permitted by statutory regulation or exceeds the permitted use, you will need to obtain permission directly from the copyright holder.

To view a copy of this licence, visit http://creativecommons.org/licenses/by/4.0/.